Available online at www.sciencedirect.com

jmr&t Journal of Materials Research and Technology

journal homepage: www.elsevier.com/locate/jmrt

Original Article

Non-linear dynamic finite element analysis of micro-strut lattice structures made by laser powder bed fusion

Ondřej Červinek [a,*], *Heinz Pettermann* [b], *Melanie Todt* [b], *Daniel Koutný* [a], *Ondřej Vaverka* [a]

[a] *Institute of Machine and Industrial Design, BUT Brno, Technická 2896/2, 616 69 Brno, Czech Republic*
[b] *Institute of Lightweight Design and Structural Biomechanics, TU Wien, Gumpendorfer Straße 7, 1060 Vienna, Austria*

ARTICLE INFO

Article history:
Received 23 February 2022
Accepted 11 April 2022
Available online 15 April 2022

Keywords:
Laser powder bed fusion
Lattice structure
Split hopkinson bars test
Impact test
Dynamic loading
Finite element analysis

ABSTRACT

The development of additive manufacturing technologies enables the production of a new type of porous materials for the absorption of mechanical energy. These are, for example, metallic lattice structures produced by laser powder bed fusion. The structures can be made from a wide range of alloys, achieve high specific energy absorption, and can be manufactured as hybrid parts with conventional bulk components. To effectively develop lattice structures, it is necessary to complement experimental tests with simulations using the finite element method (FEM) performed under conditions of increased loading velocities. Therefore, this study focuses on the development of the FEM modelling strategy that reflects the effect of strain rate sensitivity of the base material (SS316L) and the most significant geometrical imperfections of the manufacturing process. The strain rate is reflected by the Cowper-Symonds constitutive law, which parameters are determined by the dynamic tensile test on Hopkinson split bars. The imperfections are captured by optical digitalization. The significance of the Cowper-Symonds parameters and geometric imperfections are studied independently, whereas agreement with the experiment is observed. Tests are performed for several lattice structures with different strut orientations and velocities to evaluate the versatility of the proposed approaches. A good correlation between computational and experimental results in terms of energy absorption is found for structures with an experimentally determined strut diameter and the proposed Cowper-Symonds input parameters.

* Corresponding author.
E-mail address: Ondrej.Cervinek@vut.cz (O. Červinek).
https://doi.org/10.1016/j.jmrt.2022.04.051

1. Introduction

Lightweight porous materials have become interesting in many industrial fields such as aerospace, transportation, biomedical engineering, and defence [1,2]. Properties such as low thermal conductivity, acoustic absorption, mechanical vibration damping, and topology adaptation for high energy absorption have been required for these materials [3–5]. The possibility of their production by additive manufacturing (AM) has introduced various architectures of porous materials with improved mechanical properties [6]. Their deformational behaviour could be adjusted according to specific requirements [7,8]. The most common porous materials are cellular structures that have regularly repeated cubic cells [9]. They can be manufactured as a single part together with bulk elements and designed for a precisely defined load case [10,11]. A frequently used AM technology is laser powder bed fusion (LPBF) that allows the processing of different materials, for example, stainless steel 316L [12], titanium alloy Ti_6Al_4V [13], or aluminium alloy $AlSi_{10}Mg$ [14,15].

Regardless of the material or technology used, it has been found that mechanical properties can be significantly improved by adjusting the process parameters [7,16]. Unfortunately, the result of the tuning process is limited by the mechanical properties of the parent material. When considering strut systems, properties decrease even more as defects are more pronounced in thin geometries [4,17]. Changes in internal lattice arrangement have also led to different types of deformation [18]. This behaviour has been associated with the bending or stretching dominated character of the lattice structure [19,20]. The approach can be applied to many structures, but, except for topology (connectivity of the struts and the degrees of freedom), it does not take into account other factors such as direction and loading conditions or node shape [21].

The performance of the structure can be further improved by local modifications of the struts. For example, a structure with slightly parabolic tapered struts could achieve higher stiffness and lead to a lighter configuration [7]. Similarly, square honeycomb configurations can achieve higher strength and energy absorption efficiency under dynamic loading if thin walls are replaced with deformed strut shapes with equivalent relative density [5]. Another way to improve performance is to redesign the geometry of the entire structure with implicit mathematical equations using tapered struts and fillets at the central nodes to increase mechanical properties [6,22]. Further improvement of energy absorption could be achieved when relative density is continuously changed. This can be done by changing the dimensions of the smallest unit element called a unit cell, in the loading direction [13].

It is necessary to perform detailed finite element analyses (FEA) of the deformation response to predict the mechanical properties of the lattice structures [16,23]. The computational model must contain information about the behaviour of the parent material obtained by mechanical tests on the thin strut [24,25]. Cervinek et al. [26] have already discussed a detailed analysis of the material models used for the lattice structure.

The higher the loading rates and the larger the deformations, the more complex the constitutive law must describe the behaviour. Higher velocities are associated with the propagation of shock waves, significant inertial forces, and an increase in adiabatic temperature [27,28]. The simple approach uses the properties of specially shaped tensile samples with multiple struts tested on modified Hopkinson bars to obtain material parameters used in the Cowper-Symonds (C-S) law [29] as a function of the strain rate. A more sophisticated constitutive law uses the Johnson-Cook equation, which considers large strains, high loading rates, and an adiabatic temperature rise together with the failure criterion [30,31]. It is possible to neglect the adiabatic increase in temperature for a lower strain rate loading using the simplified Johnson-Cook law [32,33].

The model of the geometry that represents the structure in the simulation can be defined in different ways depending on its complexity. The most effective method uses a balanced simplification of the geometry created by the beam elements (based on the theory of Timoshenko [34] or Belytschko-Schwer [32]). The beams usually have circular cross-sections with diameters given by nominal CAD data [25,35]. However, the simulation accuracy is not very high because the model suffers from several inaccuracies in the strut geometry, the definition of the nodal connection, and the contact. An improvement in the accuracy of the Timoshenko beam element model is possible by artificially increasing the stiffness of the structural nodes [36]. A stiffness correction is made in the vicinity of the vertices using elements with artificially increased Young's modulus [21,37]. With this approach used, the beam connection better represents the actual connection of the struts, which behaves more like a spherical domain than a single point. In addition, the element diameters in these domains are increased to compensate for the larger mass of the melted material caused by a material overlap in the nodes. An advantage of beam elements is the ability to analyse larger structures with less computational effort.

In addition, increased simplification is possible [12,15,38] by replacing each unit cell with one or more solid cubic elements. The elements represent the effective properties of the structure under mechanical loading (homogenization). The next approach uses solid tetrahedral elements to model the geometry of the struts with real strut connections [16,37,39].

The purpose of this study is to explore the structural simulations of lattice structures' dynamic loading. The simulation has to consider the effects of the strain rate and the actual cross-section of the struts, which have usually been treated separately. For one of the elementary structures, the range of velocities is set from quasi-static to high-velocity loading. The simulations are compared with experiments of structures made of stainless steel by laser powder bed fusion.

2. Materials and methods

To achieve the main objectives of the study, it is necessary to perform a series of procedures related to dynamic compressive and tensile mechanical testing, optical digitalization, and finite element analysis. The most important processes are described in the following sections (see Fig. 1).

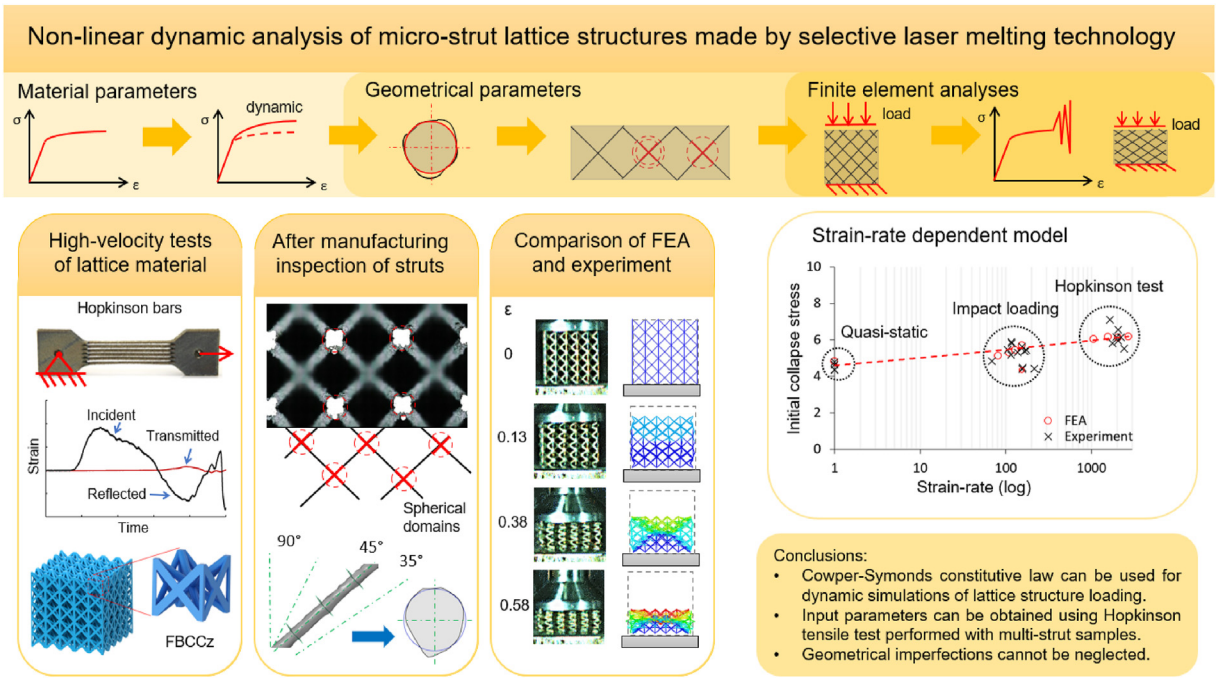

Fig. 1 – Scheme of the most important process steps of the research.

Stainless steel 1.4404 (SS 316L) metal powder (TLS Technik GmbH, Bitterfeld-Wolfen, Germany) is chosen to produce all samples on the SLM 280^{HL} machine (SLM Solutions, Lübeck, Germany). The distribution of powder particles, chemical analysis, and process parameters were presented in the previous study [28]. The manufacturing process parameters remained the same to preserve consistent mechanical properties.

2.1. *Dimension and shape analysis*

Groups of struts with a length of 20 mm (nominal diameter 0.6 mm) are manufactured at the corners of the building platform to inspect the actual dimensions of the struts in the lattice structures. The layout should reflect potentially different conditions across the platform caused by the irregular flow of inert gas. The different angles of the struts are used to cover all angles that appeared within the manufactured structures (90°, 45°, and 35.26°). The struts were subjected to an optical digitalization process. An ATOS Triple Scan optical scanner (GOM GmbH, Braunschweig, Germany) with an MV170 lens is used (calibration is carried out according to VDI/VDE 2634). Samples were coated with titanium dioxide powder before scanning to prevent the reflection of light projection (coating thickness approximately 5 μm [40]).

The strut scans are evaluated using the GOM Inspect v8.0 software (GOM GmbH, Braunschweig, Germany). Measurements are evaluated at several regularly spaced cross-sections of the strut (see Fig. 2 a)). Each measurement is made using circle that approximated the actual cross-section of the struts based on the Gaussian best fit method (3-point sigma, see Fig. 2 b)) [41].

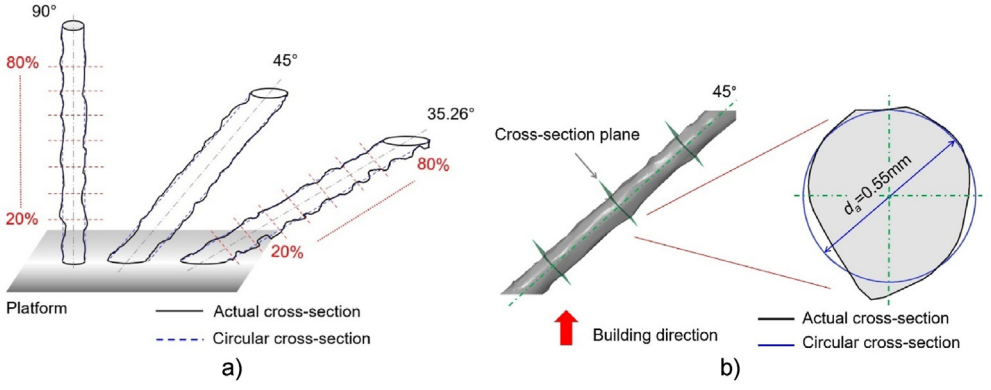

Fig. 2 – a) height of the cross-sections, b) derivation of different cross-sections.

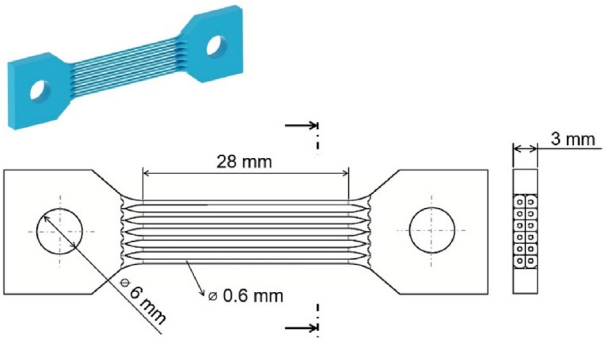

Fig. 3 – Multi-strut tensile sample for SHBT.

2.2. *Split hopkinson bars test (SHBT)*

Conventional tensile samples manufactured according to common standards (ISO, DIN 50 125) have been found to not accurately represent the mechanical properties of the lattice structure [41,42]. Therefore, strut tensile samples with a nominal strut diameter equal to the lattice structure struts are used (strut diameter 0.6 mm, 12 struts, see Fig. 3) [4,42,43].

Dynamic tensile tests are carried out using modified split Hopkinson tensile bars (see Fig. 4, SVS FEM, Brno, Czech Republic) to determine the mechanical properties of 316L stainless steel under dynamic loading. The initial loading velocity was 30 m s^{-1}. The samples are attached to the bars of the device using a bolt connection. The incident and transmission bars are made of structural steel (with Young's modulus 205 GPa, density 7850 kg m^{-3}, and Poisson's ratio 0.3). Semiconductor strain gauges EP140-3-35-G (VTS Zlín s.r.o., Zlín, Czech Republic) with a nominal resistance of 350 Ω, a grid length of 3 mm, and a k-factor of +140 are placed in pairs in the middle of both bars. The strain gauges are connected in the half Wheatstone bridge configuration to eliminate any flexural stress on the bars. The signal emitted from the Wheatstone bridge is strengthened with amplifiers. The signal is further recorded with a high-speed oscilloscope with a recording frequency of 10 MHz.

At the beginning of the SHBT, the striker bar impacts the loading block, indicating negative pulse propagation [29]. The pulse travels along the parallel bars until it reaches the second block. Then an elastic wave is reflected, causing a positive stress load in the incident bar. It generates tension wave propagation through the incident bar into the sample from the loading side. When the elastic wave arrives at the interface sample-incident bar, a part of the tension wave reflects as a compression wave from the interface, while the other part continues to propagate along with the sample and into the transmit bar until the sample breaks. Massive wave reflection is caused due to the impedance difference between the sample and the incident bar. The sample loading time is given by the time it takes for the tension wave to reflect itself in the form of an unloading compression wave from the transmit bar free end and for this unloading wave to interact with the sample.

In the next step, a similar device based on the principle of moving bars toward each other is used for high-velocity dynamic compression of structured cubes, as described by Nolting et al. [44].

The signals coming from the gauges are evaluated in the form of engineering stress σ, strain rate $\dot{\varepsilon}$, and strain ε, using the following known Eq. (1–3) [29,44,45] (assuming for one dimensional stress wave theory):

$$\sigma = \frac{A_0 E_0}{A}\varepsilon_t(t) \tag{1}$$

$$\dot{\varepsilon} = -\frac{2C_0}{L}\varepsilon_r(t) \tag{2}$$

$$\varepsilon(t) = -\frac{2C_0}{L}\int_0^t \varepsilon_r dt \tag{3}$$

where $\varepsilon_t(t)$ represents the transmitted wave, whilst $\varepsilon_r(t)$ represents a reflected wave. A_0 and E_0 represent the cross-sectional area and the Young's modulus of the bars, while A indicates the cross-sectional area summed over all struts in the multi-strut sample. In addition, L indicates the initial length of the sample in loading direction, whilst C_0 indicates the elastic wave velocity given by Eq. (4) [44]:

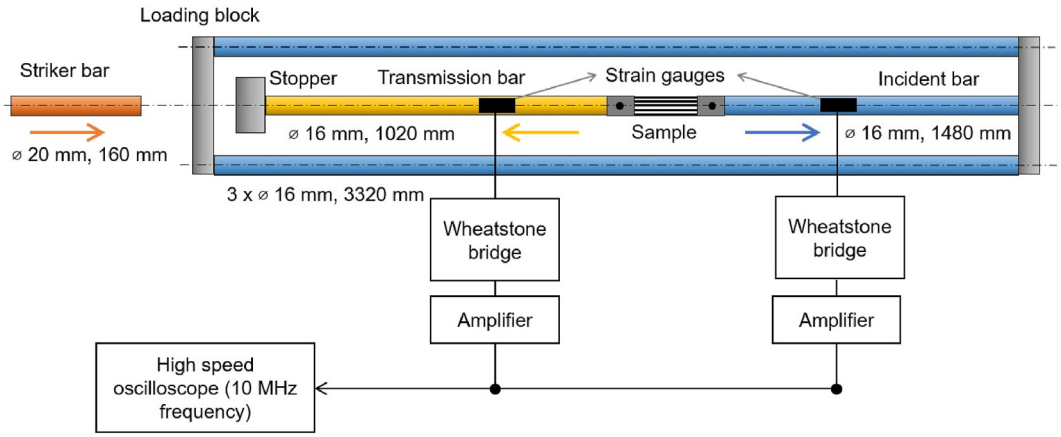

Fig. 4 – Schematic picture of Hopkinson bars used for dynamic tensile tests.

Table 1 – C-S proposed parameters.

Authors	D [s^{-1}]	q [-]	Description
Langdon & Schleyer [46]	429–2 721	4.1–5.8	Standard bulk samples, strain rates 10^{-4}-50 s^{-1}
Burgan [47]	240	4.74	Sheets with thickness 10 mm
Gümrük [29] (1)	4 851,9	4.078	To 100 s^{-1}, based on yield stress
Gümrük [29] (2)	80 736,69	5.0075	To 6600 s^{-1}, based on yield stress
Gümrük [29] (3)	$252 \cdot 10^6$	8.054	Up to 6600 s^{-1}, based on max. tensile stress
Gümrük [29] (4)	$17 \cdot 10^6$	12	Estimation

$$C_0 = \sqrt{\frac{E_0}{\rho_0}} \tag{4}$$

where ρ_0 is the density of the bars.

2.3. C-S material parameters

The C-S constitutive law accounts for the basic mechanism of strain rate dependence [16,27]. It is possible to use the model because the range of relatively low velocities is applied. The formulation of the model is given by the following Eq. (5) [27]:

$$\sigma_d = \sigma_0 \left[1 + \left(\frac{\dot{\varepsilon}}{D}\right)^{1/q}\right] \tag{5}$$

where σ_d and σ_0 represent the yield or maximum tensile stress observed during the dynamic and static test, respectively, whilst D and q are constants obtained by performing curve fitting with the experimental data. Mechanical tests at different velocities, including quasi-static loading, are usually performed to obtain these constants for a specific material.

The literature shows C-S constants for different conditions obtained by curve fitting (see Table 1).

2.4. Impact test

The present study focuses on lattice structures with a cubic unit cell assembled by struts along the body diagonals or faces (see Fig. 5). These are specifically called body-centered cubic (BCC), face-centered cubic (FCC), and their modifications supplemented with vertical struts in the corners (BCCz, FCCz) or their combinations (FBCC, FBCCz). Lattice structure cubes with nominal dimensions of 20 × 20 × 20 mm and 4 mm unit cell size are designed for a dynamic compression test (5 samples of each structure). The nominal diameter of the structure strut in the CAD design is set to 0.6 mm.

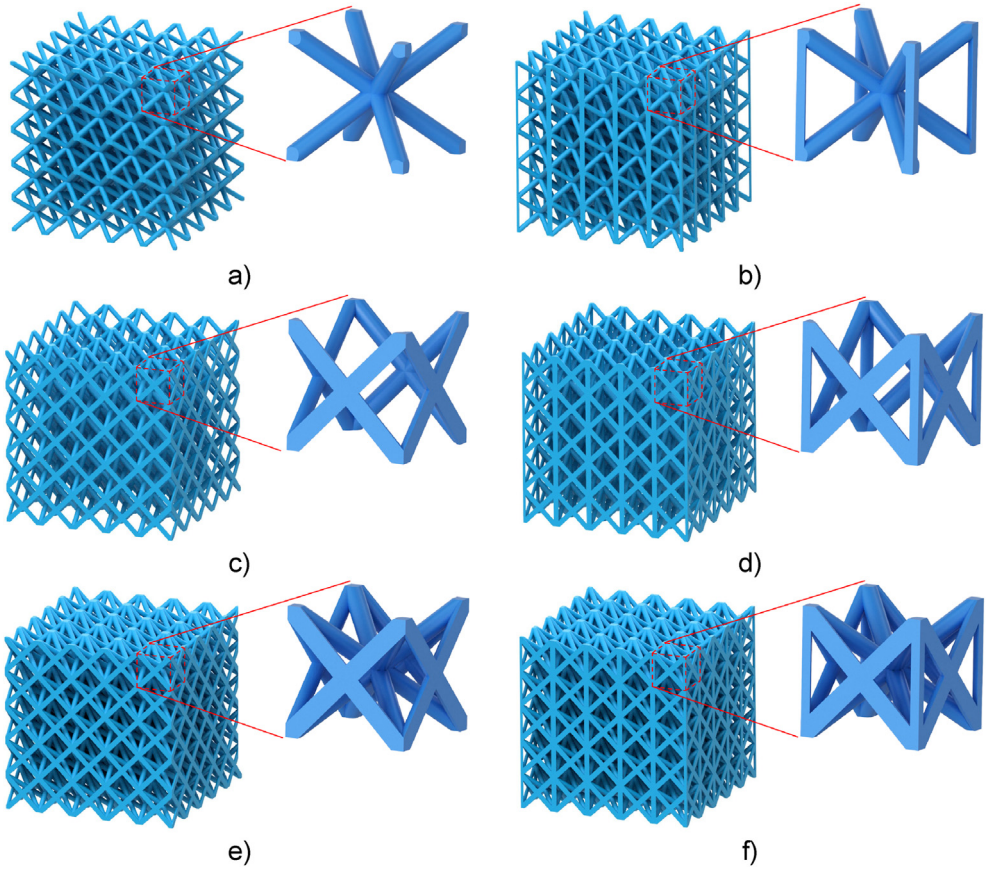

Fig. 5 – Unit cell of a) BCC, b) BCCz, c) FCC, d) FCCz, e) FBCC, and f) FBCCz lattice structure.

Drop-weight impact tests of the lattice structures are performed with the impact tester developed at the Brno University of Technology (BUT, Fig. 6). The device is equipped with a Phantom V710 high-speed camera (Vision Research, Wayne, New Jersey) and a strain gauge XY31-3/120 (HBM GmbH, Darmstadt, Germany). The strain gauge measures the reaction force during the deformation of the lattice sample, whereas the high-speed camera measures the position of the marker on the falling head to capture the deformation of the sample. A strain gauge signal is recorded using the Quantum X MX410B data acquisition system (HBM GmbH, Darmstadt, Germany) with a sampling frequency of 96 kHz. Data from the high-speed camera are recorded using Phantom Camera Control software version 3.5 (Vision Research, Wayne, NJ) with a sampling frequency of 56.808 kHz. Both records are compounded and evaluated in the MATLAB R2021a software (MathWorks, Natick, Massachusetts). The following outputs are obtained by signal evaluation: time dependence of the force reaction, deformation, and falling head velocity.

During impact tests, the overall weight of the crosshead is 13.45 kg, and the height of the drop is 1 m. For these parameters, a crosshead achieves a drop velocity of approximately 3 m s^{-1}, equal to an impact energy of 60.5 J. The testing device belongs to low-velocity test devices [14,48,49].

2.5. Finite element analysis

Numerical simulations are performed in the Explicit Dynamics module of ANSYS Workbench 20.2 (Ansys Inc., Canonsburg, Pennsylvania). The main subject of the simulations is the dynamic compression of lattice structure samples using a split Hopkinson pressure bars test and an impact test described in Sections 2.2 and 2.4.

2.5.1. Model of material

The model of material given by the elastic-plastic behaviour is determined with the quasi-static tensile test of specially shaped samples performed in the study by Cervinek [26]. The original true stress-strain response σ_T is fitted with the Hollomon Eq. (6) [5] to achieve the material parameters (strength coefficient K_H and hardening exponent n_H):

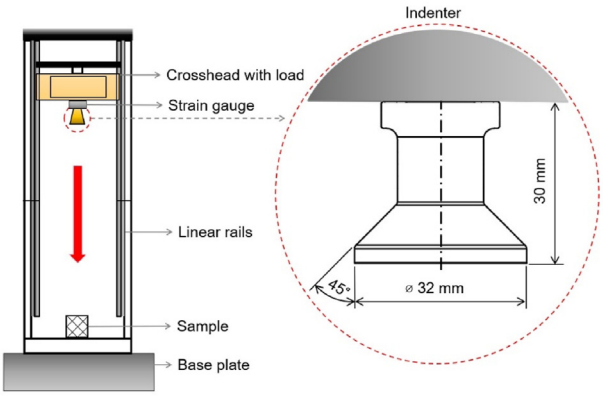

Fig. 6 – Impact tester scheme with indenter.

$$\sigma_T = \sigma_0 + K_H \varepsilon_p^{n_N} \quad (6)$$

where σ_0 is yield stress value, while ε_p is an effective plastic strain. The non-linear behaviour is then assigned to beam elements in the Workbench together with the C-S constitutive law definition [50,51] (see Table 2). The failure criterion is not considered due to the ductile properties of stainless steel, which preserves the continuity of the structure, even under large deflection [52].

2.5.2. Model of geometry

The model is created using a Python API V20 script that allows the cutting of the struts along their axis. It allows to use half or quarter cross-section at the structure surface or to define the cross-section of a random shape. All struts are further divided along the length of the axis into the mid-part and ends. Each strut consists of 2-noded beam elements (BEAM 188) based on Timoshenko beam theory, which encounters shear deformation effects. At least seven elements are used for discretization in the middle of the part. It is done according to the mesh sensitivity study performed in previous studies [14,34]. Young's modulus is ten times higher at the intersections of the struts [21]. The diameters of these elements are increased to 0.8 mm to compensate for the increase in material (see Fig. 7). The procedure ensures bending the struts rather than deforming the nodes during compression loading [53].

2.5.3. Finite element analysis setup

Except for the lattice structure, the simulation includes a top (indenter) and bottom (base) surface. Surfaces are discretized with 4-noded quadrilateral shell elements (QUAD 4 with a thickness of 3 mm) and assigned with boundary conditions [50]. The compressive loading is introduced by applying the initial velocity on an upper plate in the Y direction [displacements Ux = 0; Uy = -Y; Uz = 0] (see Fig. 7). In addition, the bottom surface is constrained in all degrees of freedom of displacement. No other constraints are applied.

A standard structural steel model of the material is assigned to the shells supplemented with ten times higher values of Young's modulus to account for the increased stiffness of the plates. The indenter surface is supplemented with an artificially increased density to represent the weight of the load head (13.45 kg). At the interfaces of the structure-indenter (vertices-face) and the structure-based plate (vertices-face), contact with a static friction coefficient of 0.15 [7,54] and a dynamic coefficient of 0.1 [2,55] is applied.

Table 2 – Material parameters of stainless-steel elastic-plastic behaviour.

Mechanical property	Value	Unit
Density of parent material ρ_s	7900	kg·m^{-3}
Young's modulus E	94000	MPa
Poisson's ratio ν	0.31	–
Yield strength σ_0	338	MPa
Strength coefficient K_H	481.45	MPa
Hardening exponent n_H	0.17	–
Ultimate tensile strength σ_{UTS}	397	MPa

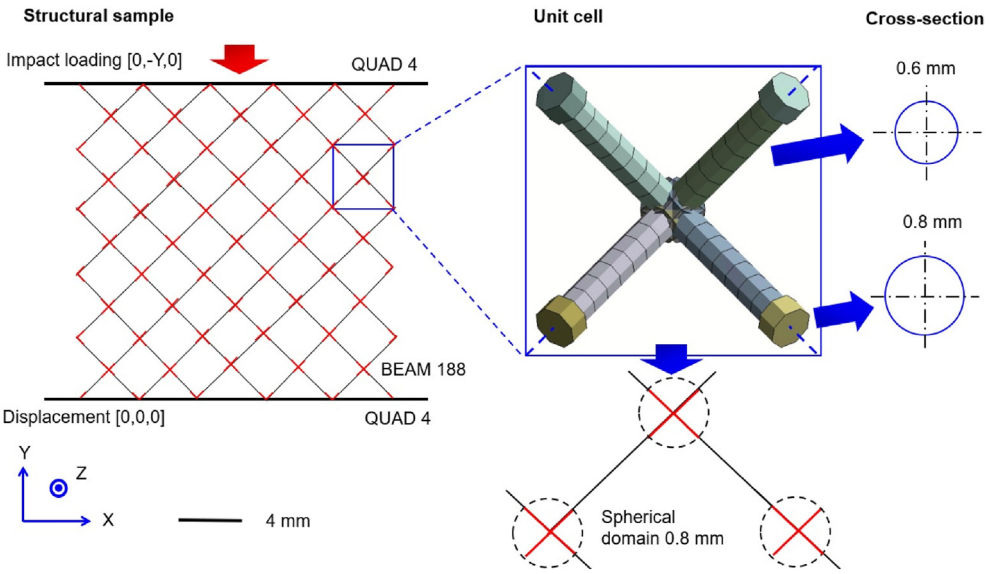

Fig. 7 – Schematic composition of the BCC lattice structure beam element model including geometrical imperfection.

3. Results and discussion

3.1. *Strut dimension analysis/samples morphology*

3.1.1. *Lattice structure samples*

After the sample manufacturing, post-processing operations and inspections are performed. Weight measurement is carried out using Sartorius MA35 with a resolution of ±0.5 mg (Sartorius, Göttingen, Germany). The measured weights are divided by the total volume of the cubic space (8000 mm^3) to obtain the actual density of the structure ρ^*. Based on the calculation, the relative density ρ'_{RE} is determined using the following Eq. (7) [10]:

$$\rho'_{RE} = \frac{\rho^*}{\rho_S} \cdot 100\% \tag{7}$$

where ρ_S is the density of parent material given by the supplier's datasheet (7 900 kg m^{-3}). The same calculation is used for the nominal CAD relative density ρ'_{CAD}, where the density of the structure is calculated by CAD software Inventor 2021 (Autodesk, San Rafael, California).

The further comparison reveals a good agreement between measured and CAD-based densities for FCC, FCCz, FBCC, and FBCCz samples (see Fig. 8 a)). On the other hand, significant differences occur between the BCC and BCCz lattice structures. Fig. 8 b) shows that the range of relative density deviations ρ'_{RED} is approximately 8% ± 1%, which is similar for all inspected structures. For most structures, the deviations are regularly distributed around the CAD-based relative density represented by zero value on a vertical axis. The different phenomena occur for BCC and BCCz lattice structures, where deviations go to positive values only. It is probably caused by the struts with an orientation of 35.26° regarding the building platform, as they incline to the most irregular aggregations. The increased transfer of heat to the powder layer beneath causes the particles in the larger area compared to the other strut orientations [16,17,28,41]. The phenomenon could occur on a smaller scale when FBCC and FBCCz structures are considered with differently oriented struts. For the standard process parameters delivered by the machine manufacturer, a negligibly low porosity value is assumed. The assumption is based on equal relative densities calculated from actual weight [56] and optical digitization.

The microscope photos (Olympus SZX7, magnification ×25, Shinjuku, Japan) show partially melted metal particles on the surface of the sample strut. Most of these particles occur at the bottom of the struts in the form of irregular clusters (see Fig. 9; arrows) due to the phenomenon mentioned above. It leads to a change in the geometry of downskin surfaces. If the phenomenon is strong enough, it can influence the shape and size of the cross section of the strut [4,56], dominantly in a direction parallel to the building direction.

3.1.2. *Single struts inspection*

The single struts are digitalized as described in Section 2.1. to determine the accurate cross-section geometry of the strut. The graph in Fig. 10 shows the diameters of struts manufactured at different angles with results organized according to a measurement position.

Based on the comparison, it can be concluded that measured diameters are smaller than the CAD-designed diameters within all inspected angles. No specific correlation was found between the change in diameters and the increase in height. Therefore, the possible increase in heat conduction at a low altitude over the building platform has no significant meaning, at least for thin struts made of SS316L up to 16 mm height above the platform (altitude of the highest cross-section). The cross-section areas of all inspected struts reach between 83.1% and 84.3% of a CAD-designed cross-section (see Table 3). This range appoints to a minimal difference in cross-sections across inspected angles but highlights the importance of differences between measured and CAD-designed geometry.

Based on the results, several points must be considered when the lattice structure geometry is prepared:

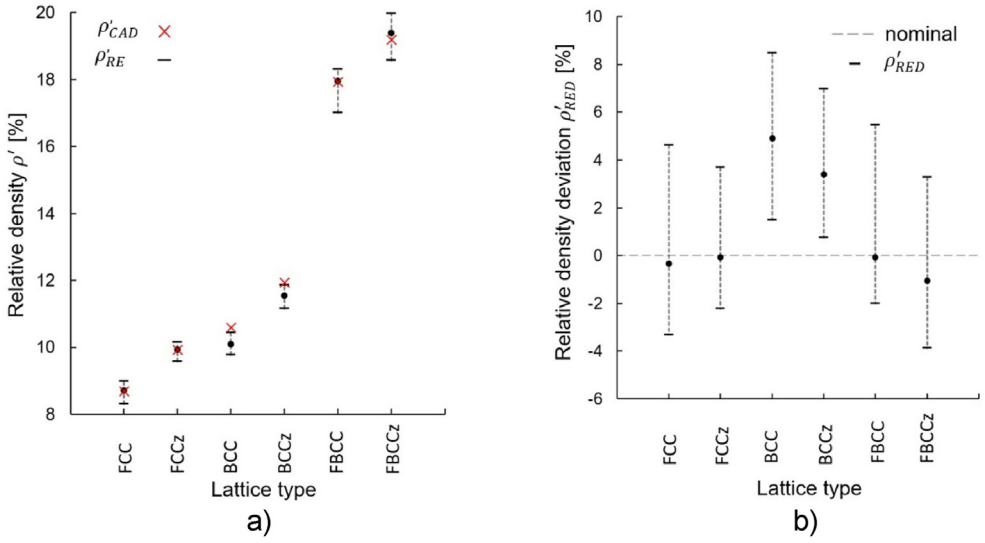

Fig. 8 – a) Comparison of measured and CAD based densities; b) deviation in relative density.

- It is possible to neglect the differences between the diameters of the struts built at different angles since the average variation is less than 3%.
- If the geometry of struts is represented by a circular cross-section based on measurements, the nominal dimension reduced by -0.05 mm can be used (see Table 3).
- The negligible range of measured strut diameters could indicate a similar influence of the laser on differently oriented struts positioned in the corners of the platform. Therefore, the mutual position of the sample-laser source can have a greater influence on the final geometry than strut orientation.
- The measurements show that the cross-sectional shape tends to certain non-circularities that can be approximated by an ellipse, which was already discussed in Cervinek et al. [26]). However, the significance of this imperfection is less important and, therefore, is not discussed within the study.

3.2. *SHBT evaluation*

Fig. 11 gives an example of the results obtained by the high-velocity tensile test described in Section 2.2. The relatively low amplitude of the initiated signal produces excessive noise.

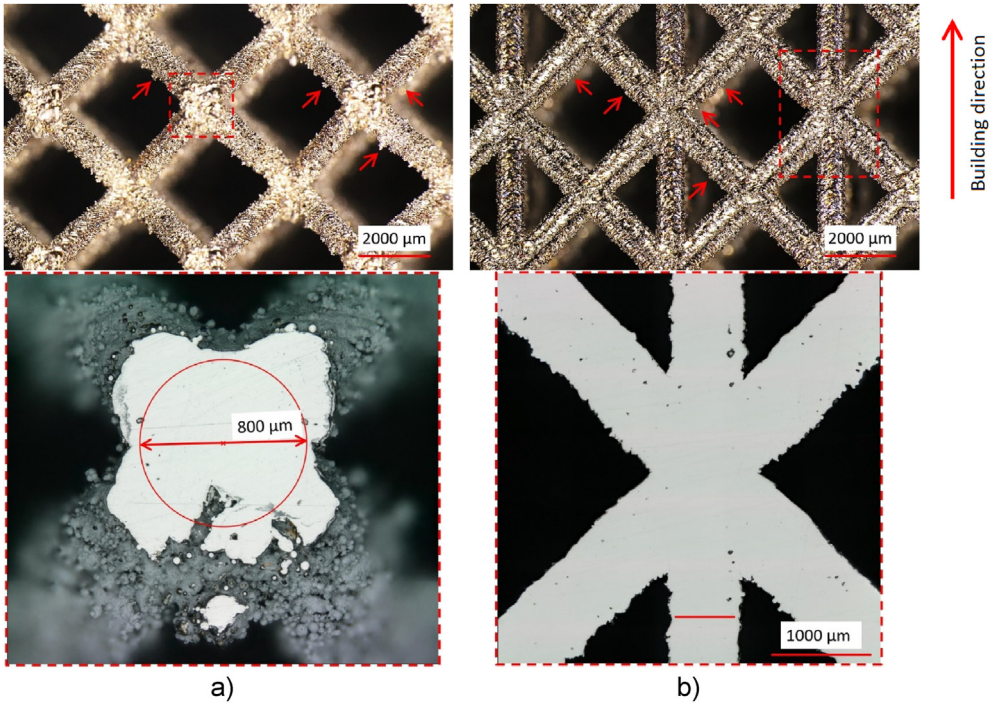

Fig. 9 – Details of manufactured a) BCC and b) FCCz structure.

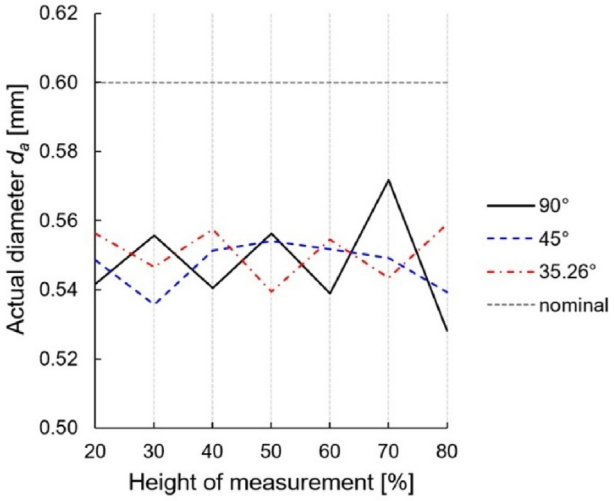

Fig. 10 – Actual strut diameter with circular approximation.

Table 3 – Results of single strut dimension measurement.

Angle [°]	Average actual diameter d_a [mm]	Cross-section area [mm^2]	Compared to nominal [%]
90	0.548	0.236	83.3
45	0.547	0.235	83.1
35.26	0.551	0.238	84.3

Therefore, the signal is cut after the first reflection to obtain readable information. The low amplitude of the transmitted signal is associated with the large difference in impedance at the sample–bar interfaces. Therefore, the signals captured on the incident bar and the transmit bar are amplified. Sample fastening conditions should be investigated in detail in the future to decrease this effect.

The response of the lattice structure in terms of acting stress, strain, and strain rate is evaluated using Eq. (1–3). The results are compared in terms of the ultimate tensile strength σ_{UTS}, maximal strain ε_{MAX}, and maximal strain rate $\dot{\varepsilon}_{MAX}$. A comparison of σ_{UTS} and quasi-static testing in a previous study

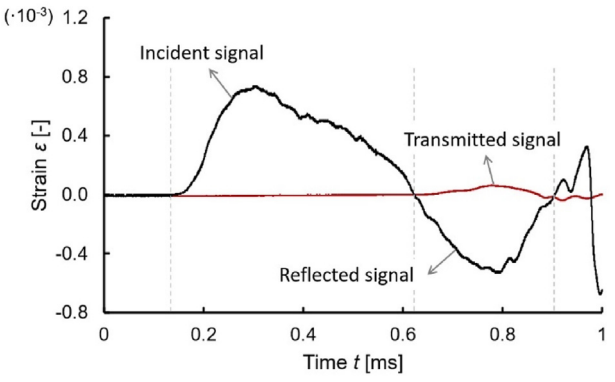

Fig. 11 – An example of SHBT result showing the incident, reflected, and transmitted strain signals with time.

Table 4 – Properties given by the Split Hopkinson tensile test of multi-strut samples.

Sample No. [-]	σ_{UTS} [MPa]	$\dot{\varepsilon}_{MAX}$ [s^{-1}]	ε_{MAX} [-]
1	597	193	0.069
2	573	196	0.075
3	557	292	0.168
4	530	226	0.032
5	522	208	0.050
Average	556	223	0.079

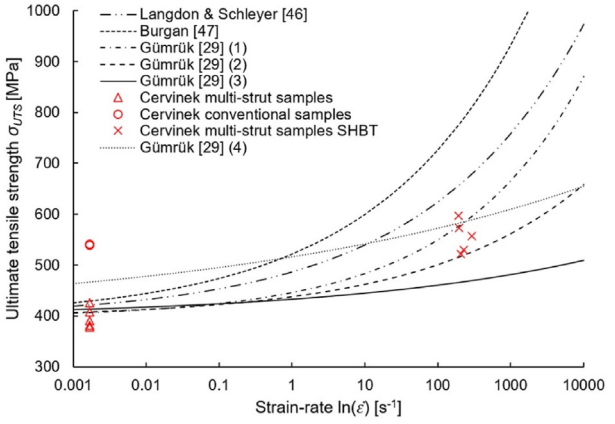

Fig. 12 – Comparison of strain rate dependent curves of the C-S equation using experimental data.

conducted with similar samples shows a 28% increase (see Table 2 and Table 4) [26].

In the next step, material data determined in the literature are fitted to the C-S model (Eq. 5). Fig. 12 shows semi-logarithmic scale curves that use parameters found by Langdon and Schleyer [46], Burgan [47], and Gümrük [29], and the quasi-static ultimate tensile strength presented by Cervinek [26] (see Table 1 and Table 2). Differences between curves are visible even for strain rates lower than 100 s^{-1}. Based on the resulting stress levels, the curves can be divided into two groups, where two upper curves are given by constants obtained by conventional samples testing [46,47], while other curves are given by constants obtained by thin strut samples testing [29].

The graph shows good agreement between the experimental results of dynamic loading (with a loading rate of approximately 220 s^{-1}) and some of the curves based on testing of thin-strut samples. Among them are two considering higher loading rates (Gümrük (2) and Gümrük (4)). As the experimental strain rates are still relatively low, also good agreement can be seen with Gümrük (1).

The experimental results of standardized DIN samples (at a loading rate of approximately 10^{-3} s^{-1}) are added to the graph to obtain complete information about the correlation between quasi-static and dynamic testing. Their comparison shows a significant difference between the results of thin strut samples and conventional volume samples. This difference has even a greater impact on the ultimate tensile strength than the increased loading rates in the low-velocity testing regime.

The result appoints to the importance of obtaining the mechanical properties of samples designed for a specific configuration, which has been discussed in [4,28,42,56].

Based on the compliance between the suggested curves and the experimental results, the parameters D and q giving curves Gümrük (1,2,4) are used.

3.3. *Impact test evaluation*

The data recorded by a high-speed camera and a strain gauge are evaluated to give the force reaction course and the position of the indenter over time. Based on it, the velocity of the structure deformation and indenter deceleration are calculated. An engineering stress value is calculated as a force reaction divided by the initial area of the sample (400 mm^2). The strain is defined from the overall deformation of the sample divided by the initial sample height given by 20 mm. The strain rate values vary between 77 s^{-1} and 125 s^{-1} within the tested structures – the highest strain rate is measured for the BCC structure with the lowest stiffness.

Despite the equivalent loading weight, the structures achieve different stress-strain responses due to their internal strut organisation and variable relative density; Fig. 13. The graphs show that the structure deformation starts in an approximately linear manner. After reaching the critical level of stress, initial collapse stress σ_{IC} (see Appendix 1), [4,42]), the deformation of the structure starts to gradually turn into a region of progressive collapse. The level of critical stress increases with increasing stiffness in the direction of loading of the structures. The highest values are achieved within the FBCCz lattice structure with an average value of 25.22 MPa.

The region of progressive collapse characteristic of an approximately constant stress level is called the plateau stress area. This behaviour is better applicable within structures without struts that have an axis in the loading direction (see Fig. 13 a), c), and e)). Their collapse is caused by bending the struts rather than buckling failure, which manifests itself by a direct change in stress level [57].

BCC, BCCz, and FCC structures (see Fig. 13 a), b), and c)) with the lowest stiffness are loaded until contact occurred between struts in neighbouring unit cells. The state is called densification [20,58]. It is defined by deformation, at which the energy absorption efficiency is the highest [52]. The ability of the material to absorb energy has its maximum at a specific stress value. The increase in absorbed energy is less than an equivalent increase in stress when the specific value is exceeded. Optimal energy absorption can be judged by efficiency (see Fig. 13) Eq. (8) [2,5,59]:

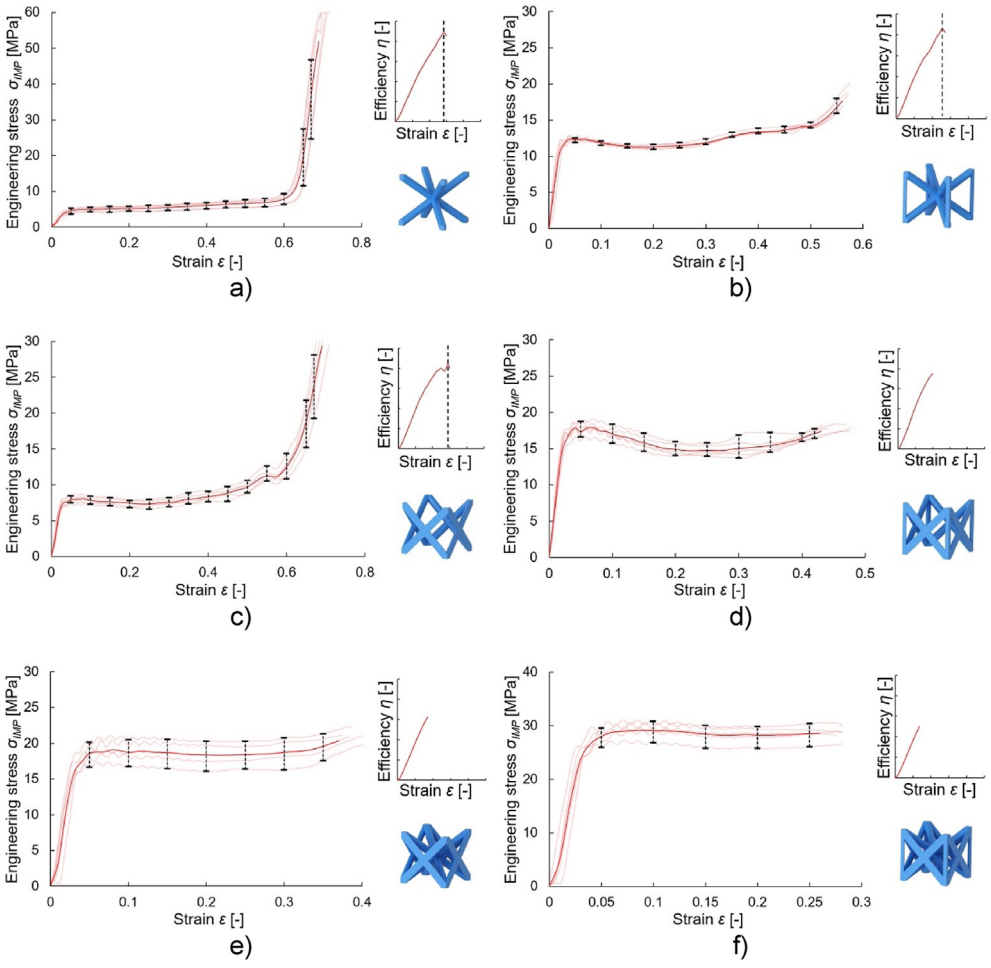

Fig. 13 – The engineering stress-strain response of a) BCC; b) BCCz; c) FCC; d) FCCz; e) FBCC; f) FBCCz lattice structures.

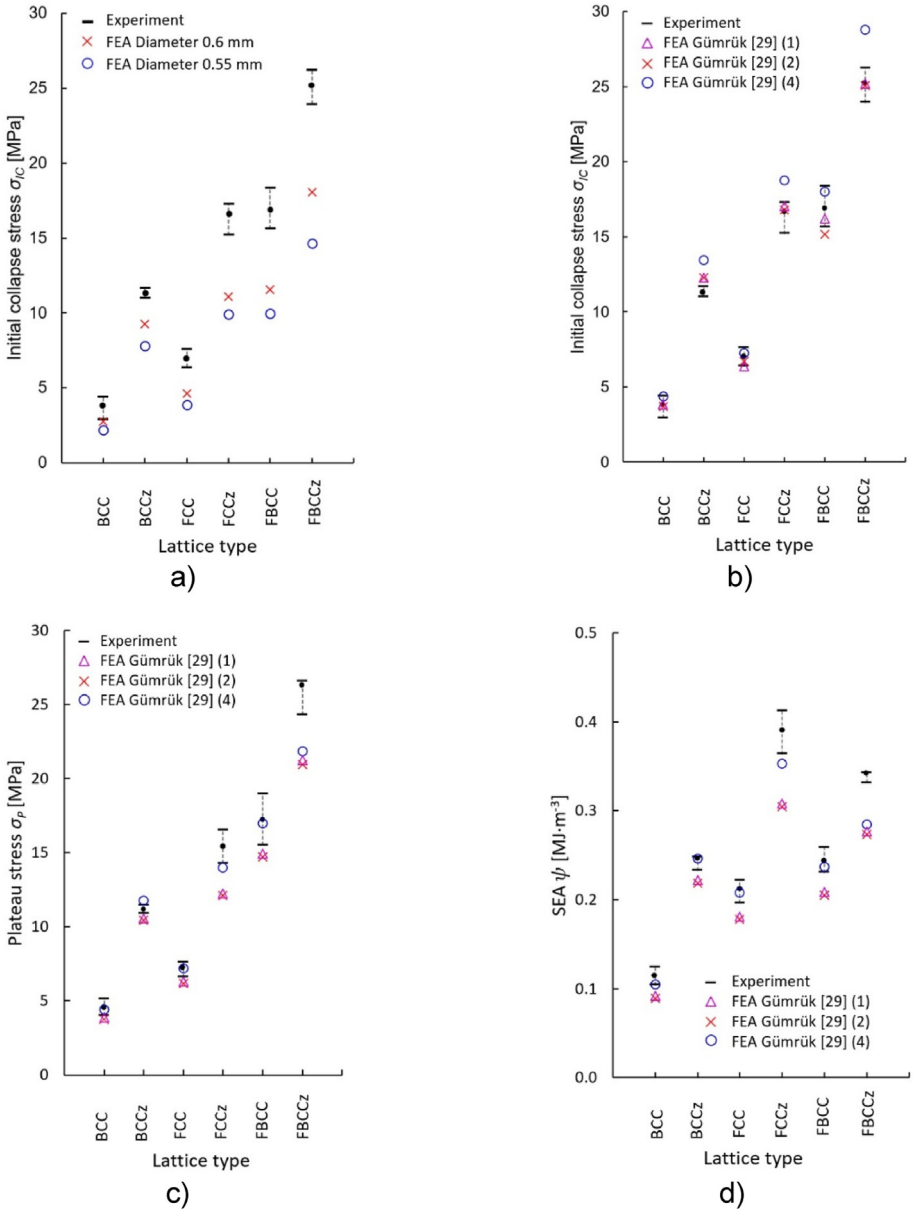

Fig. 14 – a) Comparison of initial collapse stress for nominal geometry and geometry with corrections; b) initial collapse stress with imperfection and different C-S parameters; c) plateau stress; d) SEA.

$$\eta(\varepsilon) = \frac{1}{\sigma(\varepsilon)} \int_0^{\varepsilon} \sigma(\varepsilon) d\varepsilon \tag{8}$$

The value at the beginning of densification ε_{d0} is given at the point, where energy absorption efficiency reaches its maximal value according to Eq. (9), which means:

$$\left.\frac{d\eta(\varepsilon)}{d\varepsilon}\right|_{\varepsilon=\varepsilon_{d0}} = 0 \tag{9}$$

A comparison of stress-strain response and images from the high-speed camera shows that a steep increase of stress occurred early before contact of the struts (see Fig. 13 and Appendix 1, BCC and FCC). It could be caused by the partially melted residual material between the struts, which enhances the stress response during compression loading, while within tension loading does not. The lowest strain achieves the FBCCz structure, which has the highest volume fraction. The graphs in Fig. 13 show an increasing plateau stress level when the maximal strain is decreased.

The amount of energy dissipated can be expressed as the area under engineering stress until a certain amount of deformation is achieved (up to 0.25 strain, which is approximately the strain achieved within structure deformation with

the highest stiffness). Therefore, the stress-strain response could be quantified by volume energy absorption [20] given by Eq. (10) [7]:

$$W_{25\%} = \int_0^{\varepsilon_{MAX}} \sigma(\varepsilon) d\varepsilon \tag{10}$$

In this case ε_{MAX}= 0.25. From energy absorption, the plateau stress can be calculated by Eq. (11) [60]:

$$\sigma_P = \frac{W_{25\%}}{\varepsilon} \tag{11}$$

Comparison of volume energy absorption up to 25% strain could provide only partial information about the overall absorption of the structures. With this indicator, according to expectations, the highest volume energy absorption achieves the structure with the highest stiffness. Therefore, to describe the effectivity of lattice structure configurations, volume energy absorption up to 25% strain has to be normalized by the relative density of the structure – specific energy absorption ψ (SEA). According to this metric, the efficiency of the average SEA values of the structures is compared according to Eq. (12) [7]:

$$\psi = \frac{W_{25\%}}{\rho_s \rho'_{RE}} \tag{12}$$

The FCCz configuration achieves the highest SEA ψ level (see Fig. 14 d)). The second and third most efficient structures are FBCCz and BCCz, respectively. The high SEA values for the mentioned structures are assigned to the efficiency of the struts in the loading direction. The effectivity of similar configurations can be increased if the vertical struts are prevented from early buckling. In contrast, the basic BCC lattice structure usually mentioned in many studies achieved the worst result. At least its deformation behaviour can be described by plateau stress without the stress peak typical for buckling strut failure in the loading direction.

3.4. *Comparison of FEA and experiment*

For the preparation of the simulation of the drop-weight test, two main factors are considered. The first of them is the implementation of the geometrical imperfections that occurred during the manufacturing process. Based on the measurement results in Section 3.1.2., the circular cross-section of the struts with a diameter of 0.6 mm is changed to 0.55 mm (for nodes from 0.8 mm to 0.75 mm) with the diameter approximating the actual ones. The second factor is related to the C-S strain rate sensitive constitutive law added to the material model. It is decided to investigate several parameters sets because a good agreement between the values given by the literature and the experiment has been obtained (see Fig. 12). The factors are evaluated in the dynamic simulations to quantify the influence and to compare them with experiments. Both are done separately and together.

3.4.1. *Influence of geometrical imperfection*

Fig. 14 a) shows the differences between the structures with and without geometrical corrections. Differences are expressed in terms of stress at 0.2% strain beyond linear deformation – initial collapse stress σ_{IC}. The simulation uses an elastic-plastic model of the material described in Table 2. From the comparison, it can be concluded that involving the corrections using decreasing the cross-section of the strut leads to a decrease in the initial collapse stress for all inspected lattice configurations. The cross-section decreases of about 15% causes deviation variation in the range between -12% and -25% of stress. Stress level differences show the significance of the manufacturing deviations inclusion. Therefore, it has to be considered individually for each structure as the influence on each parameter configuration differs.

3.4.2. *Influence of strain rate effects*

In the next step, the elastic-plastic nonlinear behaviour is supplemented with the C-S strain rate dependent law, and the geometrical corrections are included (diameter 0.55 mm). The response of the structures is compared in terms of the most important properties – initial collapse stress σ_{IC} (see Fig. 14 b)), plateau stress σ_P (see Fig. 14 c)), and SEA ψ (see Fig. 14 d)).

The importance of the strain rate dependent model can be observed when Fig. 14 a) FEA Diameter 0.55 mm and Fig. 14 b) FEA are compared. It can be concluded that even for low loading velocities, the strain rate dependence of SS 316L cannot be neglected. Furthermore, despite the excessively different input parameters between Gümrük (1) and Gümrük (2) (see Table 1), the results in terms of observed quantities are almost the same (see Fig. 14 b)). The significant difference

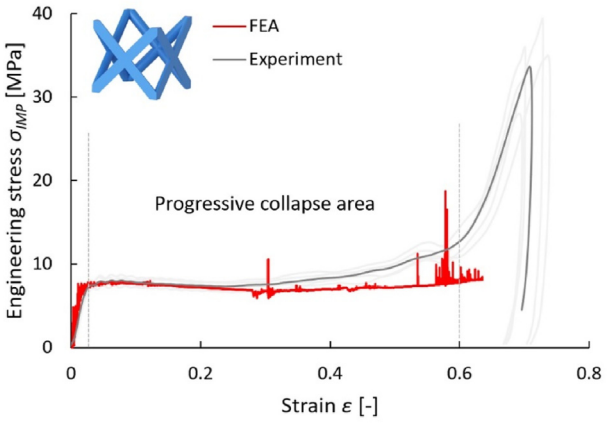

Fig. 15 – Comparison of FEA with strain rate dependency included and experiment for FCC lattice structure.

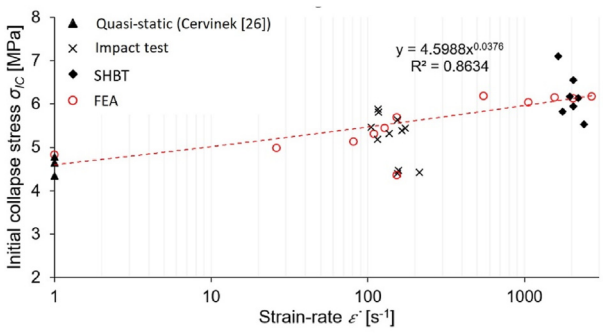

Fig. 16 – Comparison of strain rates from quasi-static to high velocities.

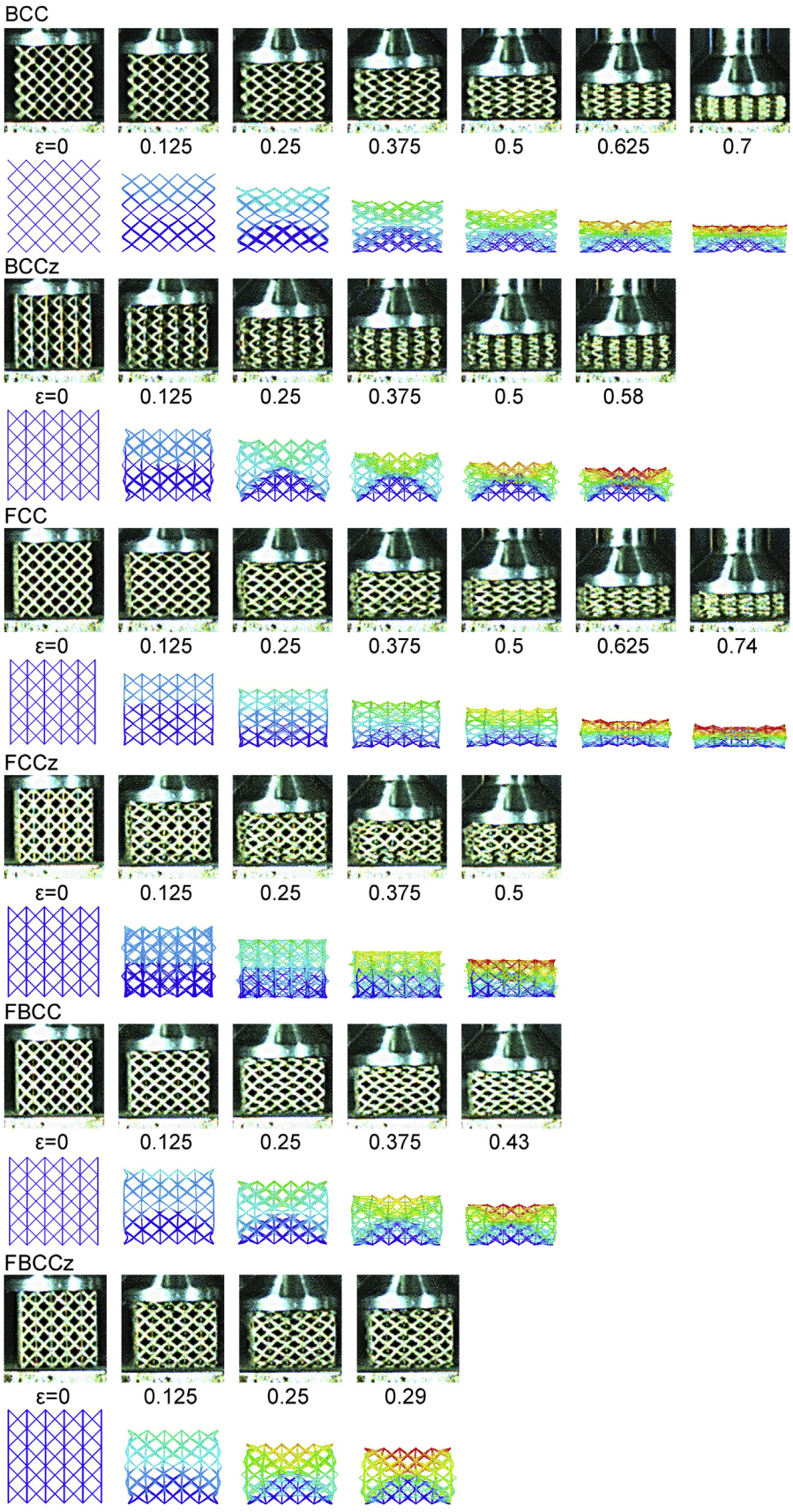

Fig. 17 – High speed images of deformation pattern of lattice structures and FEA at certain stages.

occurs when the parameters Gümrük (4) are considered. Based on the initial collapse stress comparison, it can be judged that the simulations with parameters Gümrük (1) and Gümrük (2) match better than the simulation with parameters Gümrük (4). On the contrary, if the plateau stress or SEA is compared, the simulations with Gümrük (4) parameters are closer to the experiment. It is also visible that the initial collapse stress can be predicted using FE analysis efficiently, while the energy absorption is more difficult to predict with increased structure deflection.

The simulations suffer from several simplifications when a large deformation occurs (see Appendix 1). Powder particle aggregations in the nearest area of the lattice nodes are missing in the model, which could lead to the lack of hardening during compression loading. In addition to that, the other major problem is the contact of struts in the beam element model. The true contact in the vicinity of the structural nodes is replaced by spheres of influence with artificially increased stiffness. However, when large deformations occur, the structure is deformed until the beam elements without increased stiffness touch each other. The point where the first contact of the beams occurs could be a limitation, as the only contact of the strut axis is considered in simulations. Therefore, after reaching this critical point, it cannot be expected that the simulation reflects the physically correct behaviour of the structure under loading. In the FEA reaction force response, reaching this level is manifested by excessive noise in the output signal (see Fig. 15).

In the future, the APDL commands can be used to develop a computational approach that improves the contact formulation between the struts in the lattice structure and involves a hardening effect connected with the deformation of the aggregation in the nearest area of the structure nodes.

Finally, the initial collapse stress of the BCC lattice structure deformed at different strain rates (from approximately 10^{-3} s^{-1} to $2.2 \cdot 10^{3}$ s^{-1}) is assessed. Material parameters were chosen according to the compliance of initial collapse stress with the experiment (Gümrük (1)). At several strain rates, the verification of the computational model is provided by comparison with the experiment (see Fig. 16). The FEA gives an approximately linear dependency which can be expressed by the function y. The comparison shows good agreement in the measured points and, therefore, the applicability of the model for different loading rates.

4. Conclusion

In the study, a series of computational simulations of the lattice structures dynamic loading are performed using ANSYS Workbench. The model of material is defined as the nonlinear elastic-plastic model of stainless steel 316L made by laser powder bed fusion. The plastic behaviour is defined by the Hollomon equation. The strain rate dependent behaviour given by the C-S constitutive equation is included. A new method is applied to determine the input parameters using experiments with split Hopkinson tensile bars and specially shaped thin-strut samples. The experimental results and the curves obtained from previous studies with thin struts [29] show good agreement. Optical digitization methods are used to reflect the main imperfections of the manufacturing process. Thin struts corresponding to those of the tested structures are scanned. Their cross-sections are approximated by circles to obtain a simplified shape and dimension of the strut for implementation in FEA. The models are created using a Python script, which allows us to define struts with any cross-sectional shapes. Simulations of the lattice structure impact test are performed for all configurations and compared with those of the experiment. The main conclusions of this study can be described in the following points:

1. A good agreement between the tensile tests on multi-strut samples and results given by equations from the literature is found for a low strain rate (approximately $220s^{-1}$).
2. The imperfections of the manufacturing process related to the variation in the strut cross-section cannot be neglected. For the parameters used in this study, the circular diameter reduced by about 15% can be used for all strut orientations. This leads to a deviation in the range between -12% and -25% of the stress compared to the simulation without imperfections.
3. The most efficient structure in terms of SEA is FCCz. The high efficiency is probably caused by struts with an axis in the loading direction, which are also well supported against buckling.
4. The consideration of different C-S input parameters can lead to different stress-strain responses at certain loading stages of the lattice structure. At least for the initial collapse stress, good agreement was achieved for multiple parameters and different structures.
5. The lack of contact between the struts in the beam element model seems to be the main weakness of this approach. In this study, only the contact of the beam axis is defined, which does not reflect reality if a large deflection occurs. This manifests itself in excessive noise in the force reaction response. Therefore, the contact between the beams should be redefined in the future to minimize this effect.

Declaration of Competing Interest

The authors declare that they have no known competing financial interests or personal relationships that could have appeared to influence the work reported in this paper.

Acknowledgement

This research was funded by the AKTION – bilateral cooperation in science and education between the Czech Republic and Austria in the tertiary sector, ESIF, EU Operational Programme Research, Development and Education within the research project [Architectured materials designed for additive manufacturing] grant number [CZ.02.1.01/0.0/0.0/16_025/0007304] and faculty specific research project FSI-S-20-6296. The creation of this study was allowed and supervised by the Institute of Lightweight Design and Structural Biomechanics of the TU Wien and the Institute of Machine and Industrial Design of BUT.

Appendix 1

Based on Figure 17, good compliance in the deformation pattern can be observed at small structure strains. The plastic hinges leading to locally large deformation on the diagonals are visible for the BCC lattice structure in the experiment as well as in the FEA. For the rest of the structures, the local deformation is visible on the surface of the sample. As the strain increases, the structure surfaces of the struts begin to touch, leading to a rapid increase of the acting stress. Unfortunately, this effect cannot be captured with the geometry representation of beam elements in FEA. Therefore, the FEA results should be considered valid until the strut surfaces first contact.

REFERENCES

[1] Bonatti C, Mohr D. Mechanical performance of additively-manufactured anisotropic and isotropic smooth shell-lattice materials: simulations & experiments. J Mech Phys Solid 2019. https://doi.org/10.1016/j.jmps.2018.08.022.

[2] Xiao L, Song W, Xu X. Experimental study on the collapse behavior of graded Ti-6Al-4V micro-lattice structures printed by selective laser melting under high speed impact. Thin-Walled Struct 2020. https://doi.org/10.1016/j.tws.2020.106970.

[3] Yan C, Hao L, Hussein A, Bubb SL, Young P, Raymont D. Evaluation of light-weight AlSi10Mg periodic cellular lattice structures fabricated via direct metal laser sintering. J Mater Process Technol 2014;214. https://doi.org/10.1016/j.jmatprotec.2013.12.004.

[4] Smith M, Guan Z, Cantwell WJ. Finite element modelling of the compressive response of lattice structures manufactured using the selective laser melting technique. Int J Mech Sci 2013;67:28–41. https://doi.org/10.1016/j.ijmecsci.2012.12.004.

[5] Harris JA, Winter RE, McShane GJ. Impact response of additively manufactured metallic hybrid lattice materials. Int J Impact Eng 2017;104. https://doi.org/10.1016/j.ijimpeng.2017.02.007.

[6] Zhao M, Liu F, Fu G, Zhang D, Zhang T, Zhou H. Improved mechanical properties and energy absorption of BCC lattice structures with triply periodic minimal surfaces fabricated by SLM. Materials 2018;11:2411. https://doi.org/10.3390/ma11122411.

[7] Tancogne-Dejean T, Spierings AB, Mohr D. Additively-manufactured metallic micro-lattice materials for high specific energy absorption under static and dynamic loading. Acta Mater 2016;116:14–28. https://doi.org/10.1016/j.actamat.2016.05.054.

[8] Ozdemir Z, Tyas A, Goodall R, Askes H. Energy absorption in lattice structures in dynamics: nonlinear FE simulations. Int J Impact Eng 2017;102. https://doi.org/10.1016/j.ijimpeng.2016.11.016.

[9] Singh J, Upadhyay A, Sehgal SS. A review on metallic micro lattice. Mater Today Proc 2019. https://doi.org/10.1016/j.matpr.2020.07.375.

[10] Salimon A, Bréchet Y, Ashby MF, Greer AL. Potential applications for steel and titanium metal foams. J Mater Sci 2005. https://doi.org/10.1007/s10853-005-4993-x.

[11] Tancogne-Dejean T, Mohr D. Stiffness and specific energy absorption of additively-manufactured metallic BCC metamaterials composed of tapered beams. Int J Mech Sci 2018. https://doi.org/10.1016/j.ijmecsci.2018.03.027.

[12] Labeas G, Ptochos E. Investigation of sandwich structures with innovative cellular metallic cores under low velocity impact loading. Plast Rubber Compos 2013. https://doi.org/10.1179/1743289811Y.0000000056.

[13] Xiao L, Song W. Additively-manufactured functionally graded Ti-6Al-4V lattice structures with high strength under static and dynamic loading: Experiments. Int J Impact Eng 2018;111:255–72. https://doi.org/10.1016/j.ijimpeng.2017.09.018.

[14] Geng X, Ma L, Liu C, Zhao C, Yue ZF. A FEM study on mechanical behavior of cellular lattice materials based on combined elements. Mater Sci Eng, A 2018. https://doi.org/10.1016/j.msea.2017.11.082.

[15] Labeas GN, Sunaric MM. Investigation on the static response and failure process of metallic open lattice cellular structures. Strain 2010. https://doi.org/10.1111/j.1475-1305.2008.00498.x.

[16] Gümrük R, Mines RAW. Compressive behaviour of stainless steel micro-lattice structures. Int J Mech Sci 2013. https://doi.org/10.1016/j.ijmecsci.2013.01.006.

[17] Qiu C, Yue S, Adkins NJE, Ward M, Hassanin H, Lee PD, et al. Influence of processing conditions on strut structure and compressive properties of cellular lattice structures fabricated by selective laser melting. Mater Sci Eng, A 2015. https://doi.org/10.1016/j.msea.2015.01.031.

[18] Maskery I, Tuck C, Aremu AO, Maskery I, Tuck C, Ashcroft IA, et al. A comparative Finite Element study of cubic unit cells for Selective Laser Melting. Int Solid Free Fabr Symp 2014:1238–49.

[19] Deshpande VS, Fleck NA. Isotropic constitutive models for metallic foams. J Mech Phys Solid 2000. https://doi.org/10.1016/S0022-5096(99)00082-4.

[20] Gibson LJ, Ashby MF. Cellular solids: structure and properties. 2nd ed 2014. https://doi.org/10.1017/CBO9781139878326.

[21] Luxner MH, Stampfl J, Pettermann HE. Finite element modeling concepts and linear analyses of 3D regular open cell structures. J Mater Sci 2005. https://doi.org/10.1007/s10853-005-5020-y.

[22] Yan C, Hao L, Hussein A, Young P, Raymont D. Advanced lightweight 316L stainless steel cellular lattice structures fabricated via selective laser melting. Mater Des 2014. https://doi.org/10.1016/j.matdes.2013.10.027.

[23] Crupi V, Kara E, Epasto G, Guglielmino E, Aykul H. Static behavior of lattice structures produced via direct metal laser sintering technology. Mater Des 2017. https://doi.org/10.1016/j.matdes.2017.09.003.

[24] Hasan R, Mines RAW, Shen E, Tsopanos S, Cantwell WJ, Brooks W, et al. Comparison of the drop weight impact performance of sandwich panels with aluminium honeycomb and titanium alloy micro lattice cores. Appl Mech Mater 2010;24–25:413–8. https://doi.org/10.4028/www.scientific.net/AMM.24-25.413.

[25] Ushijima K, Cantwell WJ, Mines RAW, Tsopanos S, Smith M. An investigation into the compressive properties of stainless steel micro-lattice structures. J Sandw Struct Mater 2011. https://doi.org/10.1177/1099636210380997.

[26] Červinek O, Werner B, Koutný D, Vaverka O, Pantělejev L, Paloušek D. Computational approaches of quasi-static compression loading of SS316L lattice structures made by selective laser melting. Materials 2021. https://doi.org/10.3390/ma14092462.

[27] Buchar J, Voldřich J. Terminální balistika. 1st ed. Brno: Academia; 2003.

[28] Červinek O, Vrána R, Koutný D, Paloušek D. Static and dynamic compression performance of lattice structures made by selective laser melting [n.d].

[29] Gümrük R, Mines RAW, Karadeniz S. Determination of strain rate sensitivity of micro-struts manufactured using the selective laser melting method. J Mater Eng Perform 2018;27:1016–32. https://doi.org/10.1007/s11665-018-3208-y.
[30] Banerjee A, Dhar S, Acharyya S, Datta D, Nayak N. Determination of Johnson cook material and failure model constants and numerical modelling of Charpy impact test of armour steel. Mater Sci Eng, A 2015. https://doi.org/10.1016/j.msea.2015.05.073.
[31] Grytten F, Børvik T, Hopperstad OS, Langseth M. Low velocity perforation of AA5083-H116 aluminium plates. Int J Impact Eng 2009;36:597–610. https://doi.org/10.1016/j.ijimpeng.2008.09.002.
[32] Chen Z, Wang Z, Zhou S, Shao J, Wu X. Novel negative Poisson's ratio lattice structures with enhanced stiffness and energy absorption capacity. Materials 2018;11. https://doi.org/10.3390/ma11071095.
[33] Murugesan M, Jung DW. Johnson cook material and failure model parameters estimation of AISI-1045 medium carbon steel for metal forming applications. Materials 2019. https://doi.org/10.3390/ma12040609.
[34] Ren X, Xiao L, Hao Z. Multi-property cellular material design approach based on the mechanical behaviour analysis of the reinforced lattice structure. Mater Des 2019. https://doi.org/10.1016/j.matdes.2019.107785.
[35] Labeas G, Ptochos E. Homogenization of selective laser melting cellular material for impact performance simulation. Int J Struct Integr 2015;6:439–50. https://doi.org/10.1108/IJSI-10-2014-0059.
[36] Luxner MH, Stampfl J, Pettermann HE. Linear and nonlinear numerical investigations of regular open cell structures. Am Soc Mech Eng Aerosp Div AD 2004. https://doi.org/10.1115/IMECE2004-62545.
[37] Luxner MH, Pettermann HE. Modeling and simulation of highly porous open cell structures: elasto-plasticity and localization versus disorder and defects. IUTAM Bookseries 2009. https://doi.org/10.1007/978-1-4020-9404-0_14.
[38] Pettermann HE, Hüsing J. Modeling and simulation of relaxation in viscoelastic open cell materials and structures. Int J Solid Struct 2012. https://doi.org/10.1016/j.ijsolstr.2012.04.027.
[39] 2020 ERG Aerospace Corp. ERG materials and aerospace n.d. http://ergaerospace.com/technical-data/duocel-foam-energy-absorption/.
[40] Palousek D, Omasta M, Koutny D, Bednar J, Koutecky T, Dokoupil F. Effect of matte coating on 3D optical measurement accuracy. Opt Mater 2015. https://doi.org/10.1016/j.optmat.2014.11.020.
[41] Koutny D, Engineering M, Republic C. Dimensional accuracy of single beams of AlSi10Mg alloy and 316Lstainless steel manufactured by SLM. In: Proc 5th int conf addit technol; 2014.
[42] Tsopanos S, Mines RAW, McKown S, Shen Y, Cantwell WJ, Brooks W, et al. The influence of processing parameters on the mechanical properties of selectively laser melted stainless steel microlattice structures. J Manuf Sci Eng Trans ASME 2010;132. https://doi.org/10.1115/1.4001743. 0410111–04101112.
[43] Vrána R, Cervinek O, Manas P, Koutný D, Paloušek D. Dynamic loading of lattice structure made by selective laser melting-numerical model with substitution of geometrical imperfections. Materials 2018;11. https://doi.org/10.3390/ma11112129.
[44] Nolting AE, Arsenault R, Bolduc M. Increased accuracy of SHPB test apparatus to better evaluate naval steels. Procedia Eng 2011. https://doi.org/10.1016/j.proeng.2011.04.375.
[45] Split Hopkinson pressure bar: design parameters and prediction of the experiment output. Eng Mech 2018;2018. https://doi.org/10.21495/91-8-213.
[46] Langdon GS, Schleyer GK. Unusual strain rate sensitive behaviour of AISI 316L austenitic stainless steel. J Strain Anal Eng Des 2004. https://doi.org/10.1177/030932470403900106.
[47] Burgan B. Elevated temperature and high strain rate properties of offshore steels. 2001.
[48] Banhart J. Manufacture, characterisation and application of cellular metals and metal foams. Prog Mater Sci 2001;46:559–632. https://doi.org/10.1016/S0079-6425(00)00002-5.
[49] Mohmmed R, Zhang F, Sun B, Gu B. Finite element analyses of low-velocity impact damage of foam sandwiched composites with different ply angles face sheets. Mater Des 2013;47:189–99. https://doi.org/10.1016/j.matdes.2012.12.016.
[50] Lei H, Li C, Meng J, Zhou H, Liu Y, Zhang X, et al. Evaluation of compressive properties of SLM-fabricated multi-layer lattice structures by experimental test and μ-CT-based finite element analysis. Mater Des 2019. https://doi.org/10.1016/j.matdes.2019.107685.
[51] Amani Y, Dancette S, Delroisse P, Simar A, Maire E. Compression behavior of lattice structures produced by selective laser melting: X-ray tomography based experimental and finite element approaches. Acta Mater 2018. https://doi.org/10.1016/j.actamat.2018.08.030.
[52] Zhang L, Feih S, Daynes S, Chang S, Wang MY, Wei J, et al. Energy absorption characteristics of metallic triply periodic minimal surface sheet structures under compressive loading. Addit Manuf 2018. https://doi.org/10.1016/j.addma.2018.08.007.
[53] Werner B, Todt M, Pettermann HE. Nonlinear finite element study of beams with elasto-plastic damage behavior in the post-buckling regime. Proc Appl Math Mech 2019;19:2. https://doi.org/10.1002/pamm.201900248.
[54] Lozanovski B, Leary M, Tran P, Shidid D, Qian M, Choong P, et al. Computational modelling of strut defects in SLM manufactured lattice structures. Mater Des 2019. https://doi.org/10.1016/j.matdes.2019.107671.
[55] Xie F, He X, Cao S, Mei M, Qu X. Influence of pore characteristics on microstructure, mechanical properties and corrosion resistance of selective laser sintered porous Ti-Mo alloys for biomedical applications. Electrochim Acta 2013. https://doi.org/10.1016/j.electacta.2013.04.105.
[56] Mines RAW, Tsopanos S, Shen Y, Hasan R, McKown ST. Drop weight impact behaviour of sandwich panels with metallic micro lattice cores. Int J Impact Eng 2013;60:120–32. https://doi.org/10.1016/j.ijimpeng.2013.04.007.
[57] Werner B, Červinek O, Koutný D, Reisinger A, Pettermann HE, Todt M. Numerical and experimental study on the collapse of a triangular cell under compression. Int J Solid Struct 2022. https://doi.org/10.1016/j.ijsolstr.2021.111295.
[58] Choy SY, Sun CN, Leong KF, Wei J. Compressive properties of Ti-6Al-4V lattice structures fabricated by selective laser melting: design, orientation and density. Addit Manuf 2017. https://doi.org/10.1016/j.addma.2017.06.012.
[59] Avalle M, Belingardi G, Montanini R. Characterization of polymeric structural foams under compressive impact loading by means of energy-absorption diagram. Int J Impact Eng 2001. https://doi.org/10.1016/S0734-743X(00)00060-9.
[60] Cao X, Xiao D, Li Y, Wen W, Zhao T, Chen Z, et al. Dynamic compressive behavior of a modified additively manufactured rhombic dodecahedron 316L stainless steel lattice structure. Thin-Walled Struct 2020. https://doi.org/10.1016/j.tws.2019.106586.